Indistinguishable and efficient single photons from a quantum dot in a planar nanobeam waveguide

Gabija Kiršanskė,[1] Henri Thyrrestrup,[1] Raphaël S. Daveau,[1] Chris L. Dreeßen,[1] Tommaso Pregnolato,[1] Leonardo Midolo,[1] Petru Tighineanu,[1] Søren Stobbe,[1] Rüdiger Schott,[2] Arne Ludwig,[2] Andreas D. Wieck,[2] Suk In Park,[3] Jin D. Song,[3] Andreas V. Kuhlmann,[4] Immo Söllner,[4] Matthias C. Löbl,[4] Richard J. Warburton,[4] and Peter Lodahl[1]

[1]*Niels Bohr Institute, University of Copenhagen, Blegdamsvej 17, DK-2100 Copenhagen, Denmark*
[2]*Lehrstuhl für Angewandte Festkörperphysik, Ruhr-Universität Bochum, Universitätsstrasse 150, D-44780 Bochum, Germany*
[3]*Center for Opto-Electronic Convergence Systems, Korea Institute of Science and Technology, Seoul 136-791, Korea*
[4]*Department of Physics, University of Basel, Klingelbergstrasse 82, CH-4056 Basel, Switzerland*

We demonstrate a high-purity source of indistinguishable single photons using a quantum dot embedded in a nanophotonic waveguide. The source features a near-unity internal coupling efficiency and the collected photons are efficiently coupled off-chip by implementing a taper that adiabatically couples the photons to an optical fiber. By quasi-resonant excitation of the quantum dot, we measure a single-photon purity larger than 99.4 % and a two-photon interference visibility of 62 ± 2 %, which is a measure of the degree of indistinguishability of subsequently emitted photons. A temperature-dependent study of photon indistinguishability allows pinpointing the residual decoherence processes as due to excitation-induced photon jitter and phonon decoherence. The study opens a clear pathway towards a fully deterministic source of indistinguishable photons integrated on a planar photonic chip.

A truly on-demand source of coherent single photons is the essential quantum hardware behind many photonic quantum-information applications including device-independent quantum cryptography [1, 2] and quantum simulations [3], or more daring, a full-scale photonic quantum computer [4, 5] or a quantum internet [6]. The demands on source performance depend on the actual application in mind, and currently the first proof-of-concept demonstrations emerge. Current state-of-the-art in the field is the achievement of 10-photon entanglement [7] and quantum simulations with 3–4 photons [8, 9]. A highly promising route of extending beyond this performance applies self-assembled quantum dots (QDs) as single-photon emitters [10] embedded in photonic nanostructures to enhance light-matter interaction [11]. This platform has matured significantly in recent years [11–25]. So far, much progress has been obtained on micropillar cavities and nanowires where the collected photons are coupled vertically out of the structure in a confocal microscopy setup. Planar nanophotonic waveguides offer the opportunity of increasing the single-photon coupling efficiency to near unity [18]. Importantly, the waveguide-integrated platform provides a route to on-chip photonic quantum-information processing. It remains to be demonstrated that highly coherent single photons can be generated on this platform, where the presence of surfaces near the QD may lead to decoherence [26]. Indeed the thin (~ 160 nm) and narrow (~ 300 nm) waveguide structures imply that the embedded QDs are unavoidably close to doped semiconductor material and semiconductor-air interfaces.

We present the demonstration of a highly coherent single-photon source based on an electrically controlled QD integrated in a high-efficiency nanophotonic waveguide. Pulsed quasi-resonant excitation of the QD in the waveguide is applied to deterministically operate the single-photon source, whereby the indistinguishability of the emitted photons can be directly determined as opposed to a continuous-wave excitation experiment [27, 28]. A single-photon purity larger than 99.4 % is demonstrated together with a two-photon interference visibility of 62 %. Furthermore, we present temperature-dependent indistinguishability measurements that are analyzed in terms of a microscopic model of phonon decoherence. Finally, the photons are coupled off chip to an optical fiber with a high efficiency by the implementation of a taper section. Our work paves the way for a fully deterministic source of indistinguishable photons for scalable quantum-information processing applications.

The investigated device consists of a suspended waveguide with integrated metal contacts in order to apply an external bias across the InGaAs QD to tune and stabilize the transition. The structure is terminated with a taper out-coupling section [29] for coupling the collected photons off-chip to an optical fiber, cf. Fig. 1(a). Figure 1(c) shows a scanning-electron microscope image of the sample. The 300-nm-wide suspended waveguides are fabricated on a *p-i-n* GaAs wafer (cf. Fig. 1(d) for the layer structure) using electron-beam lithography followed by dry and wet etching processes. A precise cleaving method is implemented to obtain tapers protruding from the edge of the samples such that the optical mode in the taper can freely expand without reflecting from the device substrate. For more details on the taper design,

see Supplemental Material [30]. The internal efficiency of the source is quantified by the β-factor, which is the single-photon coupling efficiency into the waveguide [11]. Fig. 1(b) displays a spatial map of the simulated β-factor in the waveguide for the two relevant dipole orientations attaining values of 84 –97 %.

For the optical measurements, the device is mounted on a three-axis piezoelectric stage in a liquid-helium bath cryostat and cooled to temperatures ranging from 4.2–26.4 K. The QD is excited with a picosecond-pulsed Ti:sapphire laser at a repetition rate of 76 MHz and focused through a microscope objective with NA=0.55. A delay is introduced in the laser path to allow for a periodic excitation with double pulses delivered with a time separation of 2.7 ns. The emitted photons are collected by a lensed single-mode fiber mounted on a separate stack of piezoelectric stages allowing for the taper-fiber spatial alignment and guided to a detection setup. A grating filtering setup is implemented (spectral resolution: 70 pm/25 GHz, transmission throughput: 27 %) in order to remove the phonon sidebands of the single photons, whereby only the spectrally narrow zero-phonon line is analyzed. The emitted photons are characterized in a Hong-Ou-Mandel interferometer [31] illustrated in Fig. 1(e). Here the spectrally filtered photons are sent to an asymmetric Mach-Zehnder interferometer designed to record the quantum interference of subsequently emitted photons. The photon indistinguishability is obtained from the two-photon auto-correlation function obtained by correlating two single-photon detectors.

The single-photon source efficiency is determined by monitoring the total number of photon counts on an avalanche photodiode and accounting for the various propagation losses in the setup. A range of different samples with outcoupling tapers was investigated. The highest observed count rate exceeded 1 MHz corresponding to an overall source efficiency of 10.3 %, which gauges the probability of creating a photon in the fiber every time the QD is triggered by an excitation pulse. Supplemental Material [30] provides further details on the source efficiency analysis. The source efficiency may be further improved by implementing evanescent coupling from the waveguide to the fiber [32].

Figure 2 displays examples of experimental data on single-photon emission from a QD in a nanophotonic waveguide. A typical emission spectrum is shown in Fig. 2(a) for a QD quasi-resonantly excited at a wavelength of 888 nm. A constant bias voltage of 0.46 V is applied to the QD in order to achieve the highest photon count rate, as deduced from the photoluminescence-voltage map, shown in Fig. 2(b). The measured autocorrelation function of $g^2(0) < 0.006$ corresponds to an excellent single-photon purity larger than 99.4 %, cf. Fig. 2(c), where $g^2(0)$ is obtained as the ratio of integrated counts of the fitted peak centered at zero time delay relative to the peak area in the uncorrelated limit

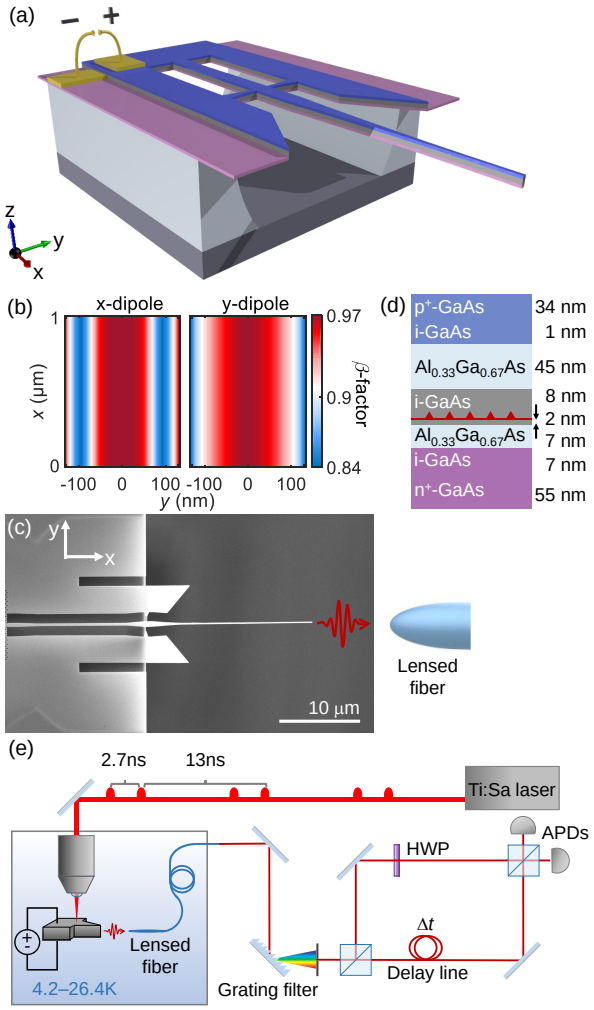

Fig. 1. Two-photon interference experiment on a QD embedded in a tapered nanobeam waveguide. (a) Sketch of the device. (b) Calculated spatial dependence of the β-factor for the two dipole orientations along the x- and y-axes of the nanobeam waveguide. (c) Scanning-electron micrograph of the waveguide sample with adiabatically tapered outcouplers. The emitted photons are collected by a lensed single-mode fiber. (d) Layer structure of the wafer used for sample fabrication, where the intrinsic layer in the middle of a *p-i-n* diode contains InGaAs QDs. (e) Schematics of the experimental setup to measure the indistinguishability of single photons consecutively emitted with variable time delay Δt. The photoluminescence of the QD is tuned via the applied electric field. The emitted photons are collected with a lensed fiber and sent to a Hong-Ou-Mandel interferometer for correlation measurements. (HWP: half-wave plate, APDs: avalanche photodiodes).

of a long time delay. This accounts for the weak blinking of emission (at a preparation efficiency of 75 %) found on a time scale of about 40 ns [33, 34].

The indistinguishability of the single photons has been tested by two-photon interference measurements of consecutively emitted photons. Figure 3(a) shows a correla-

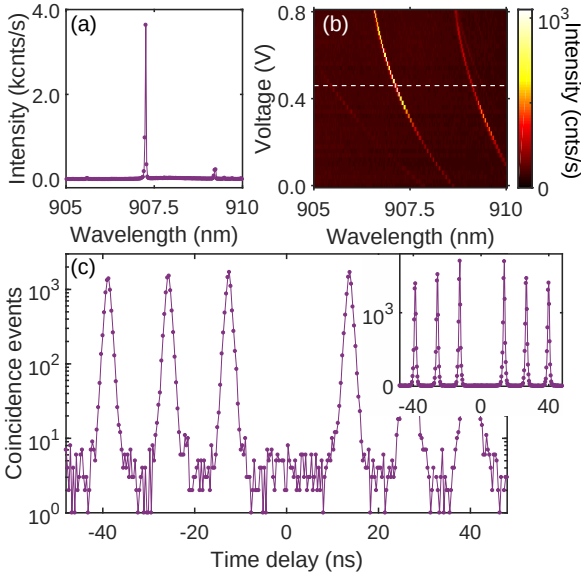

Fig. 2. Single-photon emission from an electrically controlled QD under pulsed p-shell excitation at 4.2 K. (a) Photoluminescence spectrum of the QD emitting at 907.4 nm at 0.46 V bias (indicated by the white dashed line in (b)). The width of the emission line is limited by the resolution of the spectrometer. (b) Photoluminescence map of the QD versus the applied voltage measured at an excitation level of 80 % of the saturation power. An extra line from the same quantum dot is identified at a lowered voltage and the pair most likely represent the the X^0 and X^+ transitions, respectively (c) Intensity-correlation histogram from the QD under p-shell excitation on a logarithmic scale. Nearly ideal single-photon emission is demonstrated by the vanishing multi-photon probability at zero time delay $g^2(0) < 0.006$. The inset shows the data in (c) on a linear scale.

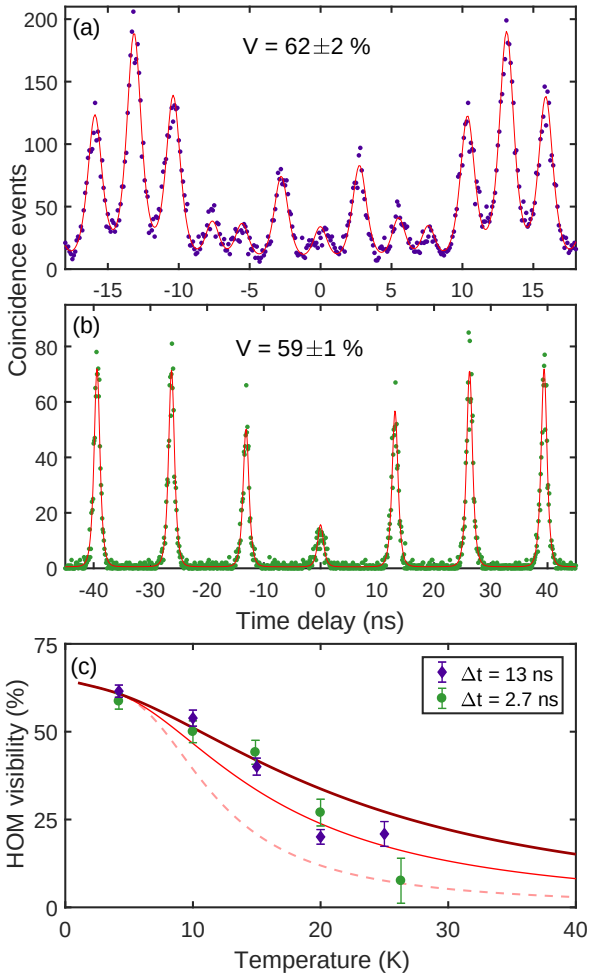

Fig. 3. Correlation histograms of photons successively emitted with a time separation of 2.7 ns (a) and 13 ns (b), respectively, measured at 4.2 K and at $0.8P_{\mathrm{sat}}$ excitation power. The data points present the raw data with no background correction integrated over 2.5 h and 1 h, respectively, and the red line shows the fit. The visibility V is extracted by fitting the data with the convolution of a single-exponential decay (QD decay) and a Voigt function (photodetector response), see Supplemental Material [30]. (c) Measured temperature dependence of the visibility for the two time separations. The error bars are calculated by error propagation of the fitted parameter errors. The curves are obtained from the theory presented in Ref. [39], and for spherical QDs of radii 2, 3, and 4 nm [40, 41] and according hole (electron) energy splitting between s- and p-shell of 15, 20, and 30 meV (30, 40, and 60 meV) [42, 43] resulting in the dashed, thin solid, and thick solid lines, respectively.

tion histogram of the two-photon coincidence events acquired. The five-peak structure of the histogram stems from the arrival of the photons at different time intervals. The central peak corresponds to the situation where two photons meet up on the beamsplitter at the same time and would vanish for completely indistinguishable photons. The degree of indistinguishability is quantified from the visibility (V) in the Hong-Ou-Mandel experiment, which can be extracted from the relative area of the central peak compared to neighboring peaks [12, 22]. We implement a rigorous fitting routine, which takes into account the exponential decay of the emitter, the measured instrument response function, and Poissonian counting statistics. This is essential in order to reliably extract V, and is not generally performed in the literature [20, 21, 24, 25, 35–37], with the notable exception of Ref. [38]. In the Supplemental Material [30] the details of the data analysis are presented, and it is found that an overestimation of V of up to 30 % may be done if the data analysis often presented in the literature is implemented. Figure 3(a) displays the data for a time delay in between photons of 2.7 ns where we obtain $V = 62 \pm 2$ %. The experiment was also repeated for a time separation of 13 ns, cf. Fig. 3(b), where we extract $V = 59 \pm 1$ %, which agrees within the error-bars of the measurement with the 2.7 ns data. The observed high degree of indistinguishability proves the promising potential of the planar waveguide platform.

The residual decoherence processes found in the measurements can be attributed to two different processes: time-jitter induced by the relaxation of the carrier from the quasi-resonant excitation to the QD ground state expressed by the rate $\Gamma_{\rm jitter}$ [44] and temperature-dependent broadening (pure dephasing rate $\Gamma_{\rm ph}(T)$) of the zero-phonon line of the QD due to interaction with phonons [45]. The visibility can be expressed as [44]

$$V = \frac{\Gamma_{\rm rad}}{(\Gamma_{\rm rad} + \Gamma_{\rm ph}(T))\,(1 + \Gamma_{\rm rad}/\Gamma_{\rm jitter})}, \qquad (1)$$

where $\Gamma_{\rm rad} = 2.3\,{\rm ns}^{-1}$ is the measured radiative decay rate of the QD. Figure 3(c) shows experimental data of the temperature dependence of the visibility. It is found to decrease significantly with temperature, which is indicative of phonon dephasing. The experimental data are compared to a theoretical model predicting the reduction of indistinguishability with temperature due to the broadening of the zero-phonon line [39] for three indicative sets of parameters, cf. Fig. 3(c). We obtain $\Gamma_{\rm jitter} = 3.7\,{\rm ns}^{-1}$ similar to literature reported values [46], where importantly this contribution may be overcome by applying resonant (π-pulse) excitation. As an important reference point the achievable indistinguishability limitation due to phonons is $V = 94\,\%$ at $T = 4\,{\rm K}$, which is consistent with linewidth measurements [47] and ultimately will be limited by the increased broadening of the zero-phonon line predicted in a 1D optical system [39]. This could be improved further by either cooling the sample more or by implementing Purcell enhancement. For instance, at $T = 1\,{\rm K}$ the indistinguishability would increase to $98.6\,\%$ or alternatively a readily achievable Purcell factor of 10 [11] would lead to $V = 98.8\,\%$ at $T = 4\,{\rm K}$.

In conclusion, we have demonstrated $> 99.4\,\%$ single-photon purity and $62\,\%$ indistinguishability of photons from a QD embedded in a planar nanoscale waveguide integrated with electrical contacts. The contribution from photon jitter may be removed by resonant excitation of the QD, whereby indistinguishability of near-unity will be attainable. Here the planar platform would favorably allow to spatially separate excitation and collection, e.g., by guiding the pump beam laterally through the structure [48] or by pumping vertically at one spot and collecting at another. This may overcome the intrinsic source efficiency limitations of $25\,\%$ found in vertical devices when implementing cross-polarization extinction in excitation [21–24]. Furthermore, a weak cavity could readily be implemented in the planar platform by terminating the waveguide end in order to achieve Purcell enhancement and reduce the role of phonon sidebands below the already modest $\sim 10\,\%$ level found for QDs in a bulk medium [11]. Combining these functionalities into a single device would eventually enable a fully deterministic and coherent single-photon source, which could subsequently be spatially demultiplexed by implementing fast switches to generate a scalable resource of single photons. The limit to the number of achievable simultaneous photons on demand with such an approach is ultimately determined by any loss processes that leads to an exponential reduction of the rate of photon generation. This constitutes an important future challenge for the research.

We acknowledge Alisa Javadi for fruitful discussions, Kasper Prindal-Nielsen for the β-factor calculations, and Tim Schröder for valuable input to the experimental setup. We gratefully acknowledge financial support from the European Research Council (ERC Advanced Grant "SCALE"), Innovation Fund Denmark (Quantum Innovation Center "Qubiz"), and the Danish Council for Independent Research. SIP & JDS acknowledge support from the KIST flagship institutional program. AVK, IS, ML & RJW acknowledge support from SNF (project 200020_156637) and NCCR QSIT. A.L. and A.D.W. gratefully acknowledge support of BMBF - Q.com-H 16KIS0109 and the DFG - TRR 160.

[1] E. Diamanti, H.-K. Lo, B. Qi, and Z. Yuan, npj Quantum Inf. **2**, 16025 (2016).
[2] N. Sangouard and H. Zbinden, J. Mod. Opt. **59**, 1458 (2012).
[3] A. Aspuru-Guzik and P. Walther, Nat. Phys. **8**, 285 (2012).
[4] P. Kok, W. J. Munro, K. Nemoto, T. C. Ralph, J. P. Dowling, and G. J. Milburn, Rev. Mod. Phys. **79**, 135 (2007).
[5] T. Rudolph, arXiv:1607.08535.
[6] H. J. Kimble, Nature **453**, 1023 (2008).
[7] X.-L. Wang, L.-K. Chen, W. Li, H.-L. Huang, C. Liu, C. Chen, Y.-H. Luo, Z.-E. Su, D. Wu, Z.-D. Li, H. Lu, Y. Hu, X. Jiang, C.-Z. Peng, L. Li, N.-L. Liu, Y.-A. Chen, C.-Y. Lu, and J.-W. Pan, Phys. Rev. Lett. **117**, 210502 (2016).
[8] J. B. Spring, B. J. Metcalf, P. C. Humphreys, W. S. Kolthammer, X.-M. Jin, M. Barbieri, A. Datta, N. Thomas-Peter, N. K. Langford, D. Kundys, J. C. Gates, B. J. Smith, P. G. R. Smith, and I. A. Walmsley, Science **339**, 798 (2013).
[9] M. A. Broome, A. Fedrizzi, S. Rahimi-Keshari, J. Dove, S. Aaronson, T. C. Ralph, and A. G. White, Science **339**, 794 (2013).
[10] P. Michler, A. Kiraz, C. Becher, W. V. Schoenfeld, P. M. Petroff, L. Zhang, E. Hu, and A. Imamoglu, Science **290**, 2282 (2000).
[11] P. Lodahl, S. Mahmoodian, and S. Stobbe, Rev. Mod. Phys. **87**, 347 (2015).
[12] C. Santori, D. Fattal, J. Vučković, G. S. Solomon, and Y. Yamamoto, Nature **419**, 594 (2002).
[13] S. Laurent, S. Varoutsis, L. Le Gratiet, A. Lematre, I. Sagnes, F. Raineri, A. Levenson, I. Robert-Philip, and I. Abram, Appl. Phys. Lett. **87**, 163107 (2005).
[14] T. Lund-Hansen, S. Stobbe, B. Julsgaard, H. Thyrrestrup, T. Sünner, M. Kamp, A. Forchel, and P. Lodahl, Phys. Rev. Lett. **101**, 113903 (2008).
[15] J. Claudon, J. Bleuse, N. S. Malik, M. Bazin, P. Jaffren-

nou, N. Gregersen, C. Sauvan, P. Lalanne, and J.-M. Gérard, Nat. Photonics **4**, 174 (2010).
[16] J. H. Prechtel, A. V. Kuhlmann, J. Houel, L. Greuter, A. Ludwig, D. Reuter, A. D. Wieck, and R. J. Warburton, Phys. Rev. X **3**, 041006 (2013).
[17] A. V. Kuhlmann, J. Houel, A. Ludwig, L. Greuter, D. Reuter, A. D. Wieck, M. Poggio, and R. J. Warburton, Nat. Phys. **9**, 570 (2013).
[18] M. Arcari, I. Söllner, A. Javadi, S. Lindskov Hansen, S. Mahmoodian, J. Liu, H. Thyrrestrup, E. H. Lee, J. D. Song, S. Stobbe, and P. Lodahl, Phys. Rev. Lett. **113**, 093603 (2014).
[19] A. V. Kuhlmann, J. H. Prechtel, J. Houel, A. Ludwig, D. Reuter, A. D. Wieck, and R. J. Warburton, Nat. Commun. **6**, 8204 (2015).
[20] M. Gschrey, A. Thoma, P. Schnauber, M. Seifried, R. Schmidt, B. Wohlfeil, L. Krüger, J.-H. Schulze, T. Heindel, S. Burger, F. Schmidt, A. Strittmatter, S. Rodt, and S. Reitzenstein, Nat. Commun. **6**, 7662 (2015).
[21] N. Somaschi, V. Giesz, L. De Santis, J. C. Loredo, M. P. Almeida, G. Hornecker, S. L. Portalupi, T. Grange, C. Antón, J. Demory, C. Gómez, I. Sagnes, N. D. Lanzillotti-Kimura, A. Lemaítre, A. Auffeves, A. G. White, L. Lanco, and P. Senellart, Nat. Photonics **10**, 340 (2016).
[22] J. C. Loredo, N. A. Zakaria, N. Somaschi, C. Anton, L. de Santis, V. Giesz, T. Grange, M. A. Broome, O. Gazzano, G. Coppola, I. Sagnes, A. Lemaitre, A. Auffeves, P. Senellart, M. P. Almeida, and A. G. White, Optica **3**, 433 (2016).
[23] H. Wang, Z.-C. Duan, Y.-H. Li, S. Chen, J.-P. Li, Y.-M. He, M.-C. Chen, Y. He, X. Ding, C.-Z. Peng, C. Schneider, M. Kamp, S. Höfling, C.-Y. Lu, and J.-W. Pan, Phys. Rev. Lett. **116**, 213601 (2016).
[24] X. Ding, Y. He, Z.-C. Duan, N. Gregersen, M.-C. Chen, S. Unsleber, S. Maier, C. Schneider, M. Kamp, S. Höfling, C.-Y. Lu, and J.-W. Pan, Phys. Rev. Lett. **116**, 020401 (2016).
[25] A. Thoma, P. Schnauber, M. Gschrey, M. Seifried, J. Wolters, J.-H. Schulze, A. Strittmatter, S. Rodt, A. Carmele, A. Knorr, T. Heindel, and S. Reitzenstein, Phys. Rev. Lett. **116**, 033601 (2016).
[26] J. Houel, A. V. Kuhlmann, L. Greuter, F. Xue, M. Poggio, B. D. Gerardot, P. A. Dalgarno, A. Badolato, P. M. Petroff, A. Ludwig, D. Reuter, A. D. Wieck, and R. J. Warburton, Phys. Rev. Lett. **108**, 107401 (2012).
[27] S. Kalliakos, Y. Brody, A. Schwagmann, A. J. Bennett, M. B. Ward, D. J. P. Ellis, J. Skiba-Szymanska, I. Farrer, J. P. Griffiths, G. A. C. Jones, D. A. Ritchie, and A. Shields, Appl. Phys. Lett. **104**, 221109 (2014).
[28] S. Kalliakos, Y. Brody, A. J. Bennett, D. J. P. Ellis, J. Skiba-Szymanska, I. Farrer, J. P. Griffiths, D. A. Ritchie, and A. J. Shields, Appl. Phys. Lett. **109**, 151112 (2016).
[29] J. D. Cohen, M. Meenehan, and O. Painter, Opt. Express **21**, 820 (2013).
[30] See Supplemental Material at [URL will be inserted by publisher] for details on the taper design, characterization of the efficiency of the single-photon source, and the HOM data analysis.
[31] C. K. Hong, Z. Y. Ou, and L. Mandel, Phys. Rev. Lett. **59**, 2044 (1987).
[32] R. S. Daveau, K. C. Balram, T. Pregnolato, J. Liu, E. H. Lee, J. D. Song, V. Verma, R. Mirin, S. W. Nam, L. Midolo, S. Stobbe, K. Srinivasan, and P. Lodahl, Optica **4**, 178 (2017).
[33] C. Santori, D. Fattal, J. Vučković, G. S. Solomon, E. Waks, and Y. Yamamoto, Phys. Rev. B **69**, 205324 (2004).
[34] M. Davanço, C. S. Hellberg, S. Ates, A. Badolato, and K. Srinivasan, Phys. Rev. B **89**, 161303 (2014).
[35] Y.-M. He, Y. He, Y.-J. Wei, D. Wu, M. Atatüre, C. Schneider, S. Höfling, M. Kamp, C.-Y. Lu, and J.-W. Pan, Nat. Nanotechnol. **8**, 213 (2013).
[36] O. Gazzano, S. Michaelis de Vasconcellos, C. Arnold, A. Nowak, E. Galopin, I. Sagnes, L. Lanco, A. Lemaître, and P. Senellart, Nat. Commun. **4**, 1425 (2013).
[37] K. H. Madsen, S. Ates, J. Liu, A. Javadi, S. M. Albrecht, I. Yeo, S. Stobbe, and P. Lodahl, Phys. Rev. B **90**, 155303 (2014).
[38] B. Kambs, J. Kettler, M. Bock, J. N. Becker, C. Arend, A. Lenhard, S. L. Portalupi, M. Jetter, P. Michler, and C. Becher, Opt. Express **24**, 22250 (2016).
[39] P. Tighineanu, C. L. Dreeßen, C. Flindt, P. Lodahl, and A. S. Sørensen, (in preparation 2016).
[40] P. W. Fry, I. E. Itskevich, D. J. Mowbray, M. S. Skolnick, J. J. Finley, J. A. Barker, E. P. O'Reilly, L. R. Wilson, I. A. Larkin, P. A. Maksym, M. Hopkinson, M. Al-Khafaji, J. P. R. David, A. G. Cullis, G. Hill, and J. C. Clark, Phys. Rev. Lett. **84**, 733 (2000).
[41] D. M. Bruls, P. M. Koenraad, H. W. M. Salemink, J. H. Wolter, M. Hopkinson, and M. S. Skolnick, Appl. Phys. Lett. **82**, 3758 (2003).
[42] S. Raymond, S. Studenikin, A. Sachrajda, Z. Wasilewski, S. J. Cheng, W. Sheng, P. Hawrylak, A. Babinski, M. Potemski, G. Ortner, and M. Bayer, Phys. Rev. Lett. **92**, 187402 (2004).
[43] J. H. Blokland, F. J. P. Wijnen, P. C. M. Christianen, U. Zeitler, J. C. Maan, P. Kailuweit, D. Reuter, and A. D. Wieck, Phys. Rev. B **75**, 233305 (2007).
[44] A. Kiraz, M. Atatüre, and A. Imamoglu, Phys. Rev. A **69**, 032305 (2004).
[45] E. A. Muljarov and R. Zimmermann, Phys. Rev. Lett. **93**, 237401 (2004).
[46] G. Reithmaier, F. Flassig, P. Hasch, S. Lichtmannecker, K. Müller, J. Vučković, R. Gross, M. Kaniber, and J. J. Finley, Appl. Phys. Lett. **105**, 081107 (2014).
[47] M. Kroner, K. M. Weiss, S. Seidl, R. J. Warburton, A. Badolato, P. M. Petroff, and K. Karrai, Phys. Stat. Sol. (b) **246**, 795 (2009).
[48] A. Muller, E. B. Flagg, P. Bianucci, X. Y. Wang, D. G. Deppe, W. Ma, J. Zhang, G. J. Salamo, M. Xiao, and C. K. Shih, Phys. Rev. Lett. **99**, 187402 (2007).

Supplemental Materials: Indistinguishable and efficient single photons from a quantum dot in a planar nanobeam waveguide

DESIGN OF OUTCOUPLING TAPER SECTION

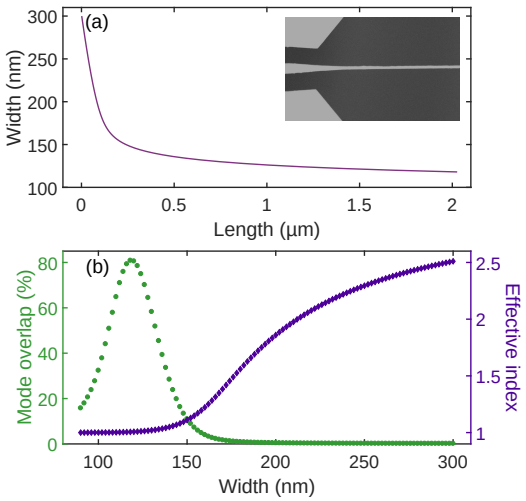

Fig. 4. Taper shape and properties extracted from the finite-element method simulation of a 160-nm-thick GaAs waveguide surrounded by air. (a) Taper profile (width as a function of length) obtained from the adiabatic rule with $\alpha = 1$ to emphasize the shape. Inset—a fragment of a scanning-electron micrograph of a fabricated taper with $\alpha = 10$. (b) Mode overlap between the waveguide mode and a Gaussian distribution of 2.5 µm mode-field diameter (green dotted curve). The maximum mode overlap serves as a guideline for the optimal taper width. Effective index as a function of the waveguide width (blue points) illustrates when the optical mode is fully leaked out into air (at a width of $\lesssim 150$ nm)

In the present work we implement a direct way to out-couple photons from a waveguide on a photonic chip to a single-mode fiber, thus discarding the need for a confocal setup. We use a direct end-fire out-coupling strategy inspired by the work of Cohen *et al.* [1], and adapted to GaAs for a working wavelength of 940 nm. The efficient coupling from a sub-micrometer sized waveguide to a 5 µm single-mode fiber core requires a redesign of the two systems to achieve good mode matching. Lensed fibers allow to reduce the fiber mode typically to a few microns, however not down to a size that matches that of a 300×160 nm waveguide mode. Tapering the waveguide along the propagation direction forces the optical mode of the waveguide to expand thereby gradually transferring the mode from GaAs with high refractive index ($n_{\mathrm{GaAs}} = 3.4$) to air. The waveguide is tapered nonlinearly, as shown in Fig. 4(a), in order to achieve the required mode diameter at a working distance of a lensed fiber. This ensures that the fiber can be operated at a safe distance from the nanophotonic waveguide during experiments.

Figure 4(b) shows the effective index of the GaAs waveguide and the mode overlap as a function of waveguide width. The maximal mode overlap is achieved when the waveguide mode is almost entirely in air while still being guided, i.e., the effective index of the waveguide is about 1. The mode overlap is maximized (80 %) for a waveguide width of 118 nm, which defines the minimum width of the waveguide taper but provides no information about its length and profile. Efficient mode conversion in the present case from a 300 nm to a 118 nm waveguide, requires that the adiabatic condition is fulfilled [2]

$$\frac{\mathrm{d}w(z)}{\mathrm{d}z} \ll n_{\mathrm{eff}}(w) - n_{\mathrm{clad}}, \tag{2}$$

where n_{eff} (n_{clad}) is the effective index of the waveguide mode (the material surrounding the waveguide). That is, the width of the waveguide along the propagation direction $w(z)$ has to change slowly to prevent coupling of the fundamental mode to higher-order or counter-propagating modes. Because of the high n_{eff} for GaAs waveguides, the effective index of the 300 nm waveguide is relatively large compared to the refractive index of air allowing to change the width of the waveguide relatively fast initially. We define the adiabatic factor α from the relation

$$\frac{\mathrm{d}w(z)}{\mathrm{d}z} = \alpha^{-1}(n_{\mathrm{eff}}(w) - 1), \tag{3}$$

where $\alpha \ll 1$ is the adiabatic condition. Setting $\alpha = 1$ at first allows to find the optimal taper shape, which can then be scaled afterwards to an arbitrary length that fulfils the adiabatic criterion. Equation (3) cannot be integrated directly because of the dependence of $n_{\text{eff}}(w)$, so instead the change in position Δz_i between two consecutive waveguide widths w_i is obtained through $\Delta z_i = \Delta w/(n_{\text{eff}}(w_i) - 1)$. This equation defines the profile of the waveguide tapered from 300 nm to 118 nm as shown in Fig. 4(a). The length of the taper is finally $\alpha \sum \Delta z_i$, which is 1.8 µm for $\alpha = 1$. The taper fabricated on the sample used in the experiments in the manuscript was designed with $\alpha = 10$.

EFFICIENCY OF THE SINGLE-PHOTON SOURCE

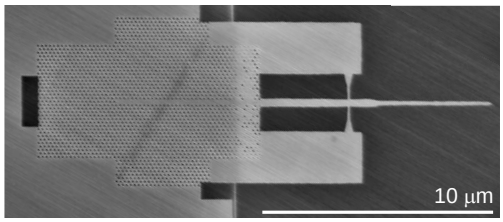

Fig. 5. Scanning-electron micrograph of a device containing a photonic-crystal waveguide coupled to a taper. The photonic-crystal waveguide is terminated on one side by a photonic-crystal-block mirror, coupled on the other side to a suspended waveguide, which is tapered into the outcoupler. The taper is design using the adiabatic parameter $\alpha = 4$.

The coupling efficiency of the planar waveguide single-photon source was thoroughly characterized on a device with no electrical contacts and is shown in Fig. 5. It was fabricated on an intrinsic 160-nm-thick GaAs membrane and it contains several waveguide sections with a photonic-crystal mirror termination on one side and waveguide taper on the other side, making the device unidirectional. The photonic-crystal waveguide has a 5-μm-long slow-light section to enhance the light-matter coupling to reach near unity β-factor [3]. The photonic-crystal waveguide is coupled to a 5-μm-long straight nanobeam waveguide, eventually tapered to a width of 118 nm with an adiabatic parameter of $\alpha = 4$ according to the design introduced in the above.

The overall photon-extraction efficiency of the device is characterized by recording the total number of detected single-photons on an APD from a QD in the photonic crystal section. A maximum count rate of ∼2 MHz is obtained above saturation (cf. Fig. 6). The corresponding detected single-photon efficiency near the saturation power is ~ 1 MHz after correcting for the multi-photon probability reflected in the final value of $g^{(2)}(0)$ shown in Fig. 6. This corresponds to an overall source efficiency of $\eta_{\text{sp}} = 10.3\,\%$. The source efficiency η_{sp} is the probability that upon excitation, the QD emits a photon that is collected by the waveguide and subsequently successfully transferred into the optical fiber. The source efficiency is obtained by accounting for all propagation losses in the fiber and detection, including APD detection efficiency (26 %), spectral filtering efficiency (30 %), and the use of two mating sleeves in between fibers (79 % each). The source efficiency is limited by a finite preparation efficiency of the QD, propagation loss in the waveguide, and the coupling efficiency off-chip. A thorough analysis of the source efficiency is presented in Ref. [4].

RELIABLE EXTRACTION OF PHOTON INDISTINGUISHABILITY FROM A PULSED HONG-OU-MANDEL EXPERIMENT

In this section, we present the fitting routine used to model the Hong-Ou-Mandel data and demonstrate the key importance of applying appropriate noise statistics for the coincidence counts and the correct line shape for the peaks in order to reliably extract the photon indistinguishabily.

The pulsed two-photon correlation histograms in Fig. 4(a) and (b) (main text) consist of a series of peaks. The peak amplitudes are determined by the relative probabilities for two photons to propagate along the different paths of a Mach-Zehnder interferometer, with either 2.7 ns or 13 ns delay lengths. The central peak near zero time delay $\Delta t = 0$ is the coincidence counts for two photons arriving on the two APDs after interfering on the last beam splitter. For completely indistinguishable photons the central amplitude is zero and the degree of indistinguishability can be quantified as the amplitude relative to the expected amplitude obtained for distinguishable photons.

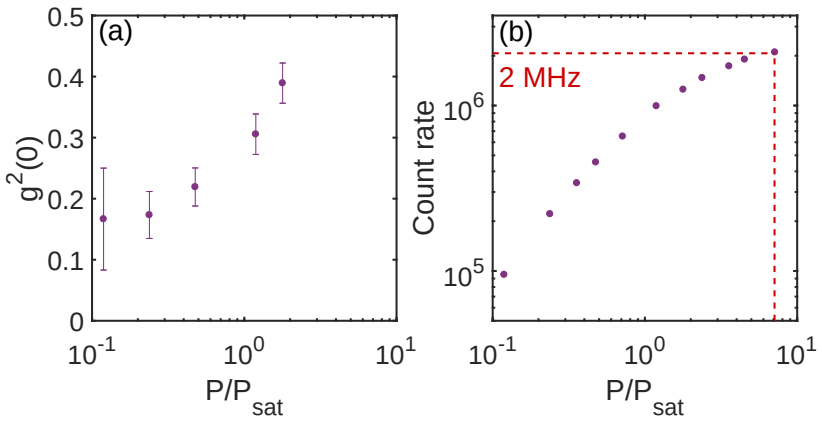

Fig. 6. (a) Autocorrelation function at zero time delay $g^2(0)$ vs excitation power measured in units of the saturation power P_{sat}. (b) Raw count rate on an avalanche photo-diode as a function of excitation power. A count rate of up to 2 MHz is observed, where about half of it stems from the QD.

As seen in the data in Fig. 4(a) (main text) for a path difference of 2.7 ns the correlation histograms consist of a five-peak cluster repeated with a 13 ns period. The visibility in this case is given by [5]

$$V_{2.7\text{ns}} = \frac{R^2+T^2}{2RT} - \frac{2A_0}{A_{+2.7\text{ns}} + A_{-2.7\text{ns}}}, \tag{4}$$

where A_0 is the area of the central peak and $A_{\pm 2.7\text{ns}}$ is the area of the two neighbouring peaks with $R = 0.46$ and $T = 0.54$ being the reflectivity and transmission of the last beam splitter. We note that no correction for the small $g^2(0) < 0.006$ is implemented in the analysis since it is an intrinsic property of the photon source and not the measurement apparatus. For the path difference of 13 ns the correlation histograms result in a set of peaks each separated by the inverse of the laser repetition rate of 13 ns. The visibility is here given as [6]

$$V_{13\text{ns}} = \frac{R^2+T^2-A_0/A}{2RT}, \tag{5}$$

where A is the average amplitude of peaks 25 ns or further away.

The five-peak cluster for 2.7 ns path difference consists of overlapping peaks resulting from the exponential QD decay with a finite rate that is on the order of the time separation between the excitation pulses. The coincidence counts therefore never reach zero, even for perfect indistinguishability, and the tail of the neighbouring peaks strongly influences the fitted amplitudes. Such data must therefore be modelled carefully in order to extract reliable values of the photon indistinguishability.

We implement a rigorous fitting routine, which takes into account the exponential decay of the emitter, the measured instrument response function (IRF), and Poissonian counting statistics. Each peak is modelled as a double-sided single exponential decay convoluted with the measured IRF. The repetition rate of the laser and the decay rate of the QD is obtained independently from the time-resolved measurements. Likewise, the ratio between pairs of neighbouring peaks is fixed by the measured beam splitter transmission and reflection. The remaining free parameters are the individual peak amplitudes, the Mach-Zehnder time delay, an overall time shift, and a background. The IRF is measured by sending a laser pulse through the detection setup and the resulting peaks are fitted with a Voigt function and a background to obtain a background-free IRF used in the convolution. The Voigt function accounts for a longer tail present in the measured IRF that is not captured by a Gaussian fit (cf. Fig. 7).

We note that the photon indistinguishability data (cf. Fig. 3 of main text) only contain few coincidence counts in time bins in-between the peaks and more importantly for the central peak, which contains the information about the indistinguishability. These low counts pose a challenge for traditional least square fitting routines that minimizes the reduced χ^2_{red}

$$\chi^2_{\text{red}} = \frac{1}{n-\nu}\sum_{i=0}^{n}\frac{(y_i - f(\Delta t_i))^2}{y_i}, \tag{6}$$

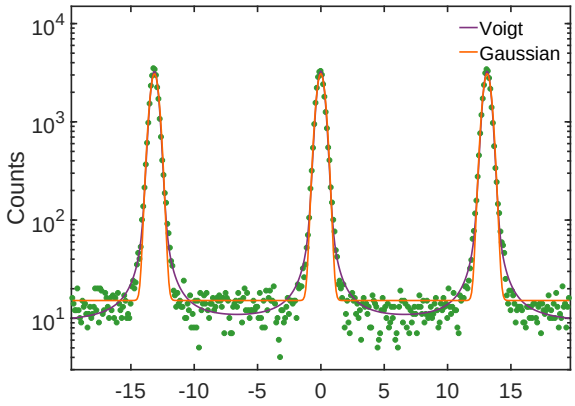

Fig. 7. The measured instrument response function (IRF) of the Hanbury Brown and Twiss setup fitted with both a Voigt (purple) and a Gaussian (orange) function using the Poission MLE described in the text. The Voigt function with it broader tail provide a superior fit to the line shape of the IRF evidenced by the smaller $\chi^2_{\mathrm{MLE}} = 2.3$ vs. $\chi^2_{\mathrm{MLE}} = 5.7$ for the Gaussian fit.

where n is the number of datapoints and ν the number of free parameters. Here y_i is the measured datapoint and $f_i \equiv f(\Delta t_i)$ is the fitting function associated with the data bin Δt_i. Minimizing Eq. (6) assumes a Gaussian noise distribution whereas the coincidence counts in reality follow a Poisson distribution[7]. Using traditional least square fitting procedures on such data is therefore known to lead to biases [8] where especially bins with $y_i = 0$ cannot be properly handled as they cause χ^2 to diverge.

To overcome the problem of low counts we instead use the maximum likelihood estimator (MLE) for the Poisson distribution and optimize that over the model parameters. The probability of measuring y_i coincidence events in the time bin Δt_i when expecting f_i on average is given by the Poisson distribution

$$P(y_i|f_i) = \frac{f_i^{y_i}}{y_i!} \exp -f_i. \tag{7}$$

Assuming independent data points the global likelihood is

$$\mathcal{L}(\mathbf{y}|\mathbf{f}) = \prod_{i=1}^{n} P(y_i|f_i). \tag{8}$$

To overcome underflow errors it is customary to minimize twice the negative logarithm of the normalized likelihood, i.e.

$$\chi^2_{\mathrm{mle}} = -2 \ln \left(\frac{\mathcal{L}(\mathbf{y}|\mathbf{f})}{\mathcal{L}(\mathbf{y}|\mathbf{y})} \right) = 2 \sum_{i=1}^{n} (f_i - y_i) - 2 \sum_{\substack{i=1 \\ y_i \neq 0}}^{n} x_i \ln \left(f_i / y_i \right). \tag{9}$$

Similarly to the reduced χ^2_{red} for least square fitting, the figure of merit χ^2_{mle} approaches one after normalizing with the number of degrees of freedom $n - \nu$ when the model accurately describes the data. In the data analysis the global minimum optimization is run 50 times with a random set of initial parameters to ensure proper convergence since the algorithm is less robust than the Levenberg-Marquardt routine used for least square fitting.

Another important point is to choose the correct line shape of the correlation function to model the data. We compare in Table I the extracted values for the two-photon-interference visibility V and the reduced χ^2_{mle} when applying the correct exponential line shape and measurement IRF compared to the case of a heuristic Lorentzian function. The "long-tail" of the Lorentzian function essentially imply that the extracted visibility V is systematically and significantly overestimated in this case. The corresponding fits to the experimental data are reproduced in Fig. 8(a). Table I summarizes the outcome of the detailed analysis of our indistinguishability data with the different approaches applied in the literature.

For the 13 ns time delay we again compare our data with Lorentzian peaks as shown in Fig. 8(b). For all the datasets the Lorentzian functions overestimate the peak heights and at the same time predict a too broad tail. As

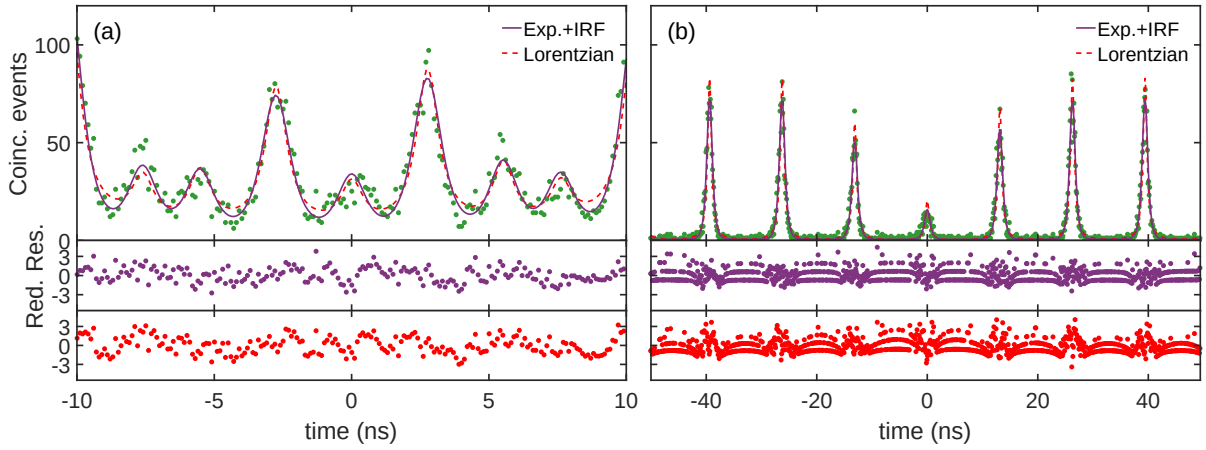

Fig. 8. Two-photon coincidence data at 4.2 K for 2.7 ns (a) and 13 ns (b) path delay. The peaks are fitted with either double-sided exponentials convoluted with the measured instruments response (solid purple) or a Lorentzian (dashed red) by optimizing the Possion MLE. The corresponding reduced residues for each fit are shown below the figures.

$\Delta t = 2.7$ ns

	Exp & IRF/MLE		Lorz/LS		Exp & IRF/LS	
T (K)	Visibility V	χ^2_{mle}	Visibility V	χ^2_{red}	Visibility V	χ^2_{red}
4.2 K	0.62 ± 0.02	1.29	0.75 ± 0.04	1.82	0.65 ± 0.03	1.42
10 K	0.54 ± 0.02	1.29	0.64 ± 0.05	1.82	0.56 ± 0.04	1.46
15 K	0.40 ± 0.02	1.47	0.50 ± 0.05	1.83	0.43 ± 0.04	1.62
20 K	0.20 ± 0.02	2.04	0.27 ± 0.05	2.00	0.23 ± 0.04	2.28
25 K	0.21 ± 0.04	1.31	0.24 ± 0.07	1.67	0.22 ± 0.06	1.53
Methods in literature	[9]		[10–12]		[5, 13–15]	

Table I. Comparison of the fitting procedure used to analyse the data of the Hong-Ou-Mandel experiment when the peaks are fitted by either double-sided exponentials convoluted with the instrument response (Exp & IRF/MLE) or Lorentzians (Lorz). The quoted errorbars are 95% confidence intervals for the parameters extracted from the fits. The reported χ^2_{mle} values are normalized by $1/(n-\nu)$. Literature references using the presented fitting routines to extract the HOM visibility in QDs. (Lorz—Lorentzian functions, LS—Least Square, MLE—Maximum Likelihood Estimator.)

evident from the small reduced residues the data points above the fitted peaks for exponential fit are within the expected errorbars for Poissonian noise. The overestimated central peak leads to overall lower visibilities, despite the overestimated side peaks, and the broad tail causes the background to be pushed below zero. The latter is not physical since only positive values are allowed in the Poisson distribution.

[1] J. D. Cohen, M. Meenehan, and O. Painter, Opt. Express **21**, 820 (2013).
[2] A. W. Snyder and J. D. Love, *Optical Waveguide Theory*, 1st ed. (Springer US, Boston, MA, 1984) p. 738.
[3] M. Arcari, I. Söllner, A. Javadi, S. Lindskov Hansen, S. Mahmoodian, J. Liu, H. Thyrrestrup, E. H. Lee, J. D. Song, S. Stobbe, and P. Lodahl, Phys. Rev. Lett. **113**, 093603 (2014).
[4] R. S. Daveau, K. C. Balram, T. Pregnolato, J. Liu, E. H. Lee, J. D. Song, V. Verma, R. Mirin, S. W. Nam, L. Midolo, S. Stobbe, K. Srinivasan, and P. Lodahl, Optica **4**, 178 (2017).
[5] N. Somaschi, V. Giesz, L. De Santis, J. C. Loredo, M. P. Almeida, G. Hornecker, S. L. Portalupi, T. Grange, C. Antón, J. Demory, C. Gómez, I. Sagnes, N. D. Lanzillotti-Kimura, A. Lemaítre, A. Auffeves, A. G. White, L. Lanco, and P. Senellart, Nat. Photonics **10**, 340 (2016).
[6] J. C. Loredo, N. A. Zakaria, N. Somaschi, C. Anton, L. de Santis, V. Giesz, T. Grange, M. A. Broome, O. Gazzano,

G. Coppola, I. Sagnes, A. Lemaitre, A. Auffeves, P. Senellart, M. P. Almeida, and A. G. White, Optica **3**, 433 (2016).
[7] P. Gregory, *Bayesian Logical Data Analysis for the Physical Sciences: A Comparative Approach with Mathematica Support* (Cambridge University Press, 2005).
[8] T. A. Laurence and B. A. Chromy, Nature Methods **7**, 338 (2010).
[9] B. Kambs, J. Kettler, M. Bock, J. N. Becker, C. Arend, A. Lenhard, S. L. Portalupi, M. Jetter, P. Michler, and C. Becher, Opt. Express **24**, 22250 (2016).
[10] O. Gazzano, S. Michaelis de Vasconcellos, C. Arnold, A. Nowak, E. Galopin, I. Sagnes, L. Lanco, A. Lemaître, and P. Senellart, Nat. Commun. **4**, 1425 (2013).
[11] M. Gschrey, A. Thoma, P. Schnauber, M. Seifried, R. Schmidt, B. Wohlfeil, L. Krüger, J.-H. Schulze, T. Heindel, S. Burger, F. Schmidt, A. Strittmatter, S. Rodt, and S. Reitzenstein, Nat. Commun. **6**, 7662 (2015).
[12] A. Thoma, P. Schnauber, M. Gschrey, M. Seifried, J. Wolters, J.-H. Schulze, A. Strittmatter, S. Rodt, A. Carmele, A. Knorr, T. Heindel, and S. Reitzenstein, Phys. Rev. Lett. **116**, 033601 (2016).
[13] Y.-M. He, Y. He, Y.-J. Wei, D. Wu, M. Atatüre, C. Schneider, S. Höfling, M. Kamp, C.-Y. Lu, and J.-W. Pan, Nat. Nanotechnol. **8**, 213 (2013).
[14] K. H. Madsen, S. Ates, J. Liu, A. Javadi, S. M. Albrecht, I. Yeo, S. Stobbe, and P. Lodahl, Phys. Rev. B **90**, 155303 (2014).
[15] X. Ding, Y. He, Z.-C. Duan, N. Gregersen, M.-C. Chen, S. Unsleber, S. Maier, C. Schneider, M. Kamp, S. Höfling, C.-Y. Lu, and J.-W. Pan, Phys. Rev. Lett. **116**, 020401 (2016).